Image Anal Stereol 2025;44:147-157 doi: 10.5566/ias.3732
Original Research Paper

THREE-DIMENSIONAL CHARACTERIZATION OF RED BLOOD CELL SHAPE VIA STEREOLOGICAL METHODS

LLUÏSA GUAL-VAYÀ

Department of Mathematics-IMAC, Universitat Jaume I, 12071-Castelló, Spain.
IUMPA, Universitat Politècnica de València, 46022-València, Spain.
e-mail: lgual@uji.es
(Received August 8, 2025; revised October 27, 2025; accepted October 28, 2025)

ABSTRACT

Red blood cells (RBCs) exhibit a variety of morphologies that reflect their physiological or pathological state. Accurate classification of these shapes is essential for clinical diagnostics and hematological research. While most current classification methods rely on two-dimensional (2D) imaging, typically obtained through smear preparations that distort the natural three-dimensional (3D) structure of RBCs, these approaches often fail to capture diagnostically relevant 3D shape information and may lead to misclassification.
In this work, we propose a novel method for 3D shape classification of RBCs based on two geometric descriptors: the spherical shape factor (F) and the bending energy (E). These descriptors are estimated directly from confocal microscopy image stacks using stereological techniques, thus avoiding the need for full 3D reconstruction. This stereological framework provides efficient, reproducible, and unbiased estimates of morphological features from sets of parallel planar sections.
We demonstrate the effectiveness of this approach on a dataset that includes both standard erythrocyte SDE cell types (discocytes, stomatocytes, spherocytes, and echinocytes) and various abnormal morphologies.

Keywords: 3D confocal microscopy, bending energy, geometric sampling, integral geometry, red blood cells, stereology.

INTRODUCTION

Erythrocytes, or red blood cells (RBCs), are blood cells responsible for oxygen transport. They contain hemoglobin, which binds oxygen, and unlike most other cells, they lack a nucleus to maximize their oxygen-carrying capacity. The erythrocyte membrane consists of a bilayer of amphiphilic molecules, each having hydrophilic and hydrophobic regions, which form a stable structure in the body's aqueous environment (Bernard, 2016).

Despite their biological complexity, erythrocyte morphology can be studied using physical principles. For example, erythrocytes can be modeled as vesicles—drops of hemoglobin enclosed by a lipid bilayer membrane. These vesicles, known as liposomes, have membranes behaving as viscous fluids capable of withstanding shear stress without rupture. The membrane is incompressible, maintaining constant area and volume. The shape of liposomes, including erythrocytes, is governed by minimization of bending energy under these area and volume constraints.

Classification of RBCs based on morphology is essential for both clinical diagnostics and hematological research. Robust and objective classification methods enhance the reliability of hematological evaluations (Bogdanova et al., 2020; Constantino, 2015; Foy, 2023). In healthy individuals, RBCs predominantly exhibit the characteristic biconcave discocyte shape, which supports mechanical flexibility and efficient gas exchange. Deviations from this canonical shape often indicate underlying disease processes and provide valuable diagnostic information.

Among RBC disorders, sickle cell disease (SCD), or sicklemia, exemplifies the clinical significance of RBC morphology and highlights the importance of shape-based diagnostic tools (Paz-Soto et al., 2025). Beyond sicklemia, various other RBC shapes associate with distinct pathological conditions (Ruef and Linderkamp, 1999). SDE cells (discocytes, stomatocytes, spherocytes, and echinocytes) represent the "classic" or most common RBC morphologies, with well-characterized relationships to cellular function and physiological or pathological states. Conversely, keratocytes, knizocytes, acanthocytes, multilobate cells, and cell clusters constitute more specialized or abnormal categories that often indicate severe damage, specific pathologies, or laboratory artifacts. Distinguishing SDE cells from these other forms is important to separate cells with normal or mildly altered morphology from those reflecting complex or severe pathological states. This distinction facilitates interpretation of cellular heterogeneity, reflecting diverse health states, mechanical stress,

or disease, and supports quantitative assessment of morphological alterations critical for monitoring disease progression or therapeutic response.

Although SDE shapes—except for "late-stage" echinocytes and spherocytes—are reversibly interconvertible (Pages et al., 2010), each SDE form corresponds to a different cellular state: discocytes are normal biconcave cells optimized for gas exchange; stomatocytes display a central concavity suggestive of membrane or osmotic alterations; spherocytes are spherical, commonly linked to hemolytic diseases due to decreased deformability and lifespan; and echinocytes bear surface spicules indicative of cell damage, osmotic stress, or pathological processes. Therefore, distinguishing among these SDE types aids in understanding the patient's physiological or pathological condition and guides specific diagnoses and treatments.

Blood samples for diagnosis typically yield planar microscopic images. These images are segmented to extract cell outlines, which are often analyzed as flat curves for classification. Classification approaches may rely on contour-derived features such as length, area, or eccentricity (Kindratenko, 2003) or treat contours as elements of geometric sets with defined distance metrics. However, flattening techniques used in sample preparation can distort 3D cell shapes, potentially causing misclassification. To address this, we propose the use of confocal microscopy, which enables 3D shape analysis.

Most RBC classification studies use squash preparations producing 2D images that alter the natural 3D morphology of RBCs, leading to shape distortions and potential clinical misinterpretation. Since many blood diseases manifest as distinct 3D shape alterations, relying solely on 2D images fails to capture vital diagnostic information, reducing reproducibility and risking transfusion safety (Waibel et al., 2022).

In contrast, three-dimensional (3D) imaging of red blood cells (RBCs) in their native suspended or fixed states preserves their complete morphology, enabling more accurate and objective phenotyping. Techniques such as confocal microscopy and digital holographic imaging provide full shape information that is strongly correlated with genetic mutations and disease states (Jaferzadeh et al., 2019; Simionato et al., 2021). Building on these advances, several recent studies have explored different 3D strategies for RBC classification. Biophysical models based on membrane-bending energy minimization and spherical harmonic expansions have successfully reproduced and distinguished characteristic morphologies such as discocytes and echinocytes (Liu et al., 2011). Digital holographic microscopy (DHM) enables 3D reconstruction of RBC profiles, where statistical clustering algorithms, including model-based clustering and K-means, have been applied to classify cells according to storage conditions (Khairy et al., 2008). Other works combine DHM with deep learning to extract geometric parameters and compute statistical indicators for diagnostic purposes (Kim et al., 2022). Furthermore, dual-stage neural networks integrating confocal microscopy and spherical harmonics spectra provide automated 3D shape recognition and classification linked to genetic blood disorders (Simionato et al., 2021). Nevertheless, achieving full 3D reconstruction from planar slices remains computationally demanding and mathematically challenging (Lin et al., 2022; Kurz et al., 2024).

To overcome these limitations, we implement stereological methods: acquiring sets of parallel, randomly oriented 2D planar images and estimating shape descriptors directly without explicit 3D reconstruction. This approach enables robust classification of RBC shapes in 3D grounded in quantitative stereology, opening new avenues for diagnostic and theragnostic applications.

Stereology is a discipline that provides efficient and unbiased estimates of quantitative surface characteristics (e.g., area, enclosed volume) from appropriate geometric sampling using planes in $\mathbb{R}^3$. Several software packages, including CAST grid, Stereology Analyzer, and Stereologer, facilitate interactive and user-friendly estimation from 3D microscopic images.

In this work, we propose a novel 3D shape characterization method applied to models of normal red blood cells. This method estimates two 3D descriptors using stereological techniques: the spherical shape factor (derived from the isoperimetric inequality) and bending energy. Based on these 3D stereological characterizations, we propose classification processes to distinguish SDE shapes from other deformed cells, using a dataset that includes both normal discocytes and various abnormal RBC morphologies. The dataset used in this study is the same as that employed in Simionato et al. (2021). In that work, the classification process included a wider range of RBC morphological classes than in our study. Therefore, the classification results reported in Simionato et al. (2021) were used as the ground truth to evaluate the performance of our stereology-based classification approach.

The paper is structured as follows. In Section 2, we describe the red blood cell dataset used for the classification tasks. Section 3, devoted to the mathematical methodology, is divided into three parts: the first defines the shape descriptors, the second derives these descriptors using integral geometry formulas, and the third presents their estimation via stereological methods. In Section 4, we compute the values of our shape descriptors for mathematical models of healthy red blood cells and perform classification using the real dataset. Finally, in Section 6, we discuss the results obtained and outline possible directions for future research.

MATERIAL

The dataset used in this study consists of confocal microscopy sections of red blood cells (RBCs) from both healthy individuals and patients with various pathologies. It is publicly available at https://doi.org/10.5281/zenodo.4670205 and was originally introduced in the work by Simionato et al. (2021). In addition to the raw dataset used in our analysis, the original study Simionato et al. (2021) also performed 3D reconstructions of the RBCs. The corresponding software code and processed data files are accessible at https://github.com/kgh-85/cytoShapeNet.

The imaging of red blood cells (RBCs) is performed using confocal microscopy with scanning along the Z-axis. As a result, the acquired images represent a stack of parallel cross-sections of the sample. The orientation of RBCs within the sample is assumed to be random; however, certain aspects of sample preparation, such as centrifugation, interactions with surfaces, and the physical properties of the fixed cells, may influence the orientation, potentially deviating from true randomness. Nonetheless, this imaging approach enables the analysis of the three-dimensional (3D) structure of RBCs based on the information captured in the sequential planar sections.

In each of these planar sections, we define the contour of the RBC. These extracted contours form the basis for estimating shape parameters that are later used to describe each cell's 3D morphology (see Figure 1).

Each 3D image of a single RBC obtained through confocal microscopy consists of 185 individual Z-slices stored as TIFF stacks, each slice having a resolution of 100 × 100 pixels. Thus, the full image volume for each cell measures 100 px × 100 px × 185 px. Each stack ideally contains one single, centered RBC, and the spacing between adjacent slices is $T = 0.85$ pixel, ensuring high-resolution sampling along the Z-axis.

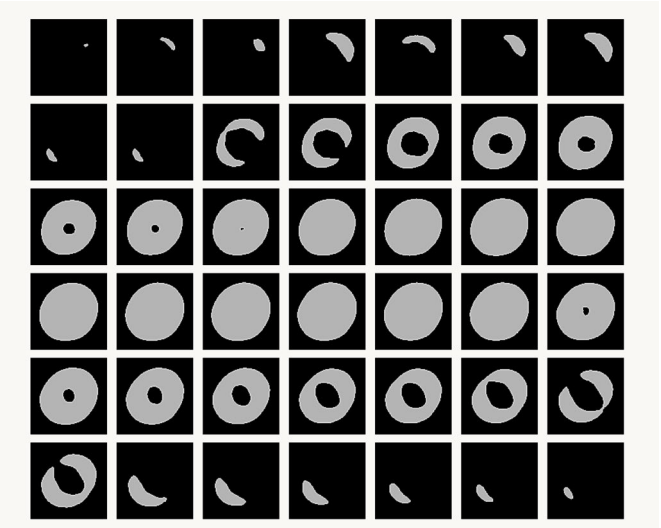

Fig. 1. *2D images of a normal single cell acquired using confocal microscopy.*

METHODS

In this section we present the mathematical methodology we developed to associate each red blood cell with a pair of shape parameters. These parameters are estimated using stereological techniques and will later be employed for RBC classification.

DIFFERENTIAL GEOMETRY OF SURFACES IN $\mathbb{R}^3$: SHAPE FACTORS

Each RBC will be modeled by a domain $D \subset \mathbb{R}^3$ whose boundary $S = \partial D$ is a regular, compact, connected surface that is homeomorphic to a 2-sphere $\mathbb{S}^2$. Therefore, we begin with an introduction to the fundamental concepts of differential geometry of surfaces (DoCarmo, 1976).

We say that a unitary vector $\vec{u}$ tangent to a surface S at a point p determines a principal direction in the tangent space T_pS if the normal curvature function achieves a maximum or a minimum at $\vec{u}$. We denote the maximum and minimum values of the normal curvature by κ_M and κ_m, respectively.

We define the Gaussian curvature of a regular surface S at a point p as

$$K(p) = \kappa_M \kappa_m.$$

Similarly, we define the mean curvature of a regular surface S at a point p as

$$H(p) = \frac{\kappa_M + \kappa_m}{2}.$$

Let S be a regular, orientable, and compact surface. Then, the Gauss–Bonnet theorem states that

$$\int_S K\,dS = 2\pi\,\chi(S), \tag{1}$$

where $\chi(S)$ denotes the Euler–Poincaré characteristic of S. It follows that if S is homeomorphic to the sphere $\mathbb{S}^2$, then no matter how "irregular" or geometrically distorted the surface may be, the Gaussian curvature K is distributed in such a way that

$$\int_S K\,dS = 4\pi, \tag{2}$$

just as it is for the standard round sphere.

Let D be a domain in $\mathbb{R}^3$ bounded by a surface S. The spatial isoperimetric inequality states that (Ritore and Sinestrari, 2010):

$$A^3(S) \geq 36\pi V^2(D), \tag{3}$$

where $A(S)$ is the surface area of S and $V(D)$ the volume enclosed by S. Equality holds if and only if D is an open ball.

Definition 1. *The **spherical shape factor** F of a domain D bounded by the surface S is defined as:*

$$F = \frac{A^3}{36\pi V^2}, \tag{4}$$

where $A = A(S)$ and $V = V(D)$.

From the isoperimetric inequality, it follows that $F \geq 1$, and equality holds if and only if D is an open ball.

Many popular surface energy functionals are inspired by classical energy functionals for curves. In this context, the bending energy for surfaces is a generalization of Bernoulli's *elastica* energy, which measures the integral of the square of curvature along a curve, i.e., $\int \kappa^2(s)\,ds$, (Gual-Vayà, 2024).

Definition 2. *The **bending energy** E of a regular surface S in $\mathbb{R}^3$ is defined as (Willmore, 2002):*

$$E = \int_S (\kappa_M^2 + \kappa_m^2)\,dS, \tag{5}$$

where κ_M and κ_m are the principal curvatures of the surface S.

Expanding the integrand gives:

$$E = \int_S (\kappa_M^2 + \kappa_m^2)\,dS = 4\int_S H^2\,dS - 2\int_S K\,dS, \tag{6}$$

where H and K are the mean and Gaussian curvatures, respectively.

According to Eq.(2),

$$E = 4\int_S H^2\,dS - 8\pi. \tag{7}$$

Let D be a domain in $\mathbb{R}^3$ bounded by a surface S. Then (Theorem 1.2 of Toda (2018)),

$$\int_S H^2\,dS \geq 4\pi, \tag{8}$$

with equality if and only if S is a sphere.

If $S = \partial D$ is the boundary of a domain, from Eq.(7), $\int_S H^2\,dS$ and E share the same minimizers. Thus, from (8), it follows that:

$$E \geq 8\pi, \tag{9}$$

with equality if and only if S is a sphere.

The spherical shape factor F and the bending energy factor E are invariant under translations, rotations, and scaling of the domain D, and for this reason, they are considered shape descriptors.

INTEGRAL GEOMETRY IN $\mathbb{R}^3$

The aim of Integral Geometry is to derive quantitative properties of a geometric object through its intersections with planes. In particular, this section presents integral formulas to compute the volume V, surface area A, and a curvature-related quantity E. The main reference for the results presented here is Santaló (1976).

Suppose that a plane (an affine plane) L_2 in $\mathbb{R}^3$ is defined by two orthonormal vectors $(\vec{e}_1, \vec{e}_2)$, and let $\vec{e}_3$ be the unit vector orthogonal to L_2. Let (θ, φ) denote the spherical coordinates corresponding to the endpoint of $\vec{e}_3$, and let ρ be the distance from the origin Q_0 of the fixed reference frame to the plane L_2. Then, the invariant density of planes L_2 under the group of motions $\mathscr{M}$ in $\mathbb{R}^3$ is given by:

$$dL_2 = \sin\varphi\,d\rho\,d\theta\,d\varphi. \tag{10}$$

The parameters vary as $\theta \in (0, 2\pi)$, $\varphi \in (0, \pi)$, and $\rho \in \mathbb{R}^+$.

Let S be a regular closed surface in $\mathbb{R}^3$ that bounds a domain D of finite volume V. From Eq. (14.69) in Santaló (1976), with $n=3$, $q=2$, and $r=2$, we obtain:

$$A(S) = \frac{2}{\pi^2} \int_{S\cap L_2\neq\emptyset} \text{Length}(S\cap L_2)\, dL_2. \tag{11}$$

Regarding the volume, for any vector $\vec{e}_3$, the Cavalieri Principle implies:

$$V(D) = \int_{-\infty}^{\infty} A(D\cap L_2)\, d\rho. \tag{12}$$

Theorem 3. *Let S be a regular, compact, connected, and orientable surface. Then:*

$$\int_{S\cap L_2\neq\emptyset} \left(\int_{S\cap L_2} \kappa^2(s)\, ds \right) dL_2 = \tag{13}$$
$$\frac{3\pi^2}{8} \int_S \left(\kappa_M^2 + \kappa_m^2\right) dS + \frac{\pi^3}{2}\chi(S).$$

Proof. At each point $p \in S\cap L_2$, from Definition 3 (page 141) and the Euler formula (page 145) of DoCarmo (1976), we have:

$$\kappa(s)\cos\phi = \cos^2 t\, \kappa_M + \sin^2 t\, \kappa_m, \tag{14}$$

where $\phi = \sphericalangle(\vec{\mathbf{n}}, \hat{N}(p))$ being $\vec{\mathbf{n}}$ the unit normal vector to the curve and $\hat{N}(p)$ the unit normal vector to the surface at p; $\{\vec{t}_M, \vec{t}_m\}$ are the principal directions at $p\in S$, $\vec{v}\in T_p(S\cap L_2)\subset T_pS$ is the unit tangent vector to the curve $S\cap L_2$, and $t = \angle(\vec{v}, \vec{t}_M)$.

Choosing the Z-axis aligned with the normal vector $\hat{N}(p)$, and letting (θ,φ) be the spherical coordinates of $\vec{e}_3$, we have, from Fig.(2), $\varphi = \frac{\pi}{2} - \phi$. Then Eq. (14) becomes:

$$\kappa(s)\sin\varphi = \cos^2 t\, \kappa_M + \sin^2 t\, \kappa_m.$$

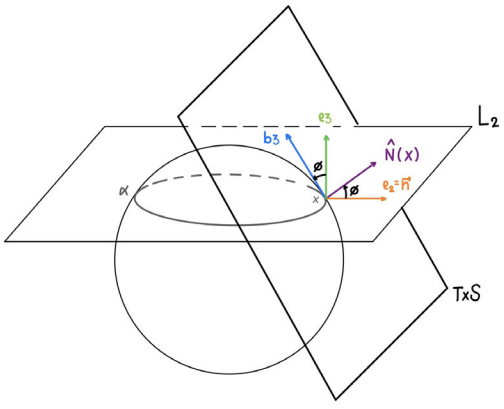

Fig. 2. *Relation between angles*

Using the identity $t = \theta + \frac{\pi}{2}$, we obtain:

$$\kappa^2(s)\sin^2\varphi = \sin^4\theta\, \kappa_M^2 + \cos^4\theta\, \kappa_m^2$$
$$+ 2\sin^2\theta\cos^2\theta\, \kappa_M\kappa_m. \tag{15}$$

From equation (14.62) of Santaló (1976), we obtain the following relation:

$$ds\, dL_2 = \cos\phi\, dS\, dL_{2[x]}, \tag{16}$$

where $dL_{2[x]} = d\mathbb{S}^2$ is the density of planes through the point p and ds and dS denote the arc length element of the curve $S\cap L_2$ and the area element of S at p, respectively.

Now, multiplying both sides of Eq. (16) by $\kappa^2(s)$, we get:

$$\kappa^2(s)\, ds\, dL_2 = \kappa^2(s)\, \sin\varphi\, dS\, dL_{2[x]},$$

and using Eq. (15):

$$\kappa^2(s)\, ds\, dL_2 = \frac{1}{\sin\varphi}\left(\sin^4\theta\, \kappa_M^2 + \cos^4\theta\, \kappa_m^2 + \right.$$
$$\left. 2\sin^2\theta\cos^2\theta\, \kappa_M\kappa_m\right) dS\, dL_{2[x]}. \tag{17}$$

Integrating over all possible values, we get:

$$I_R = \int_S \int_0^{2\pi} \int_0^{\pi/2} \left(\sin^4\theta\, \kappa_M^2 + \cos^4\theta\, \kappa_m^2 + \right.$$
$$\left. 2\sin^2\theta\cos^2\theta\, \kappa_M\kappa_m\right) d\varphi\, d\theta\, dS.$$

Thus:

$$I_R = \frac{3\pi^2}{8} \int_S \left(\kappa_M^2 + \kappa_m^2\right) dS + \frac{\pi^2}{4} \int_S \kappa_M\kappa_m\, dS.$$

Finally, applying the Gauss–Bonnet theorem (Eq. (1)) and integrating the left-hand side of Eq. (17), we conclude the proof. □

Corollary 4. *Let S be a regular surface that bounds a domain $D\subset\mathbb{R}^3$. Then:*

$$E = \frac{8}{3\pi^2} \int_{S\cap L_2\neq\emptyset} \left(\int_{S\cap L_2} \kappa^2(s)\, ds \right) dL_2 - \frac{8\pi}{3}. \tag{18}$$

Proof. In this case, $\chi(S) = 2$, and the result follows directly. □

STEREOLOGICAL ESTIMATORS

Stereological methods are used to estimate geometric parameters through appropriate geometric sampling (Cruz-Orive, 2024). In our case, the objective is to obtain estimators for the parameters V, A, and E defined in Eq.(12), Eq.(11), and Eq.(18), respectively.

To obtain an unbiased estimator of A we consider an isotropic random sampling axis defined by $u \sim UR(\mathbb{S}^2_+)$; then, a test system of planes of period $T > 0$ perpendicular to the sampling axis is defined as

$$\Lambda_{z,u} = \{L_2(z+kT,u),\, k \in \mathbb{Z}\}, \tag{19}$$

$z \sim UR[0,T), \quad u \sim UR(\mathbb{S}^2_+)$.

In this design we have considered that the direction u normal to the test planes is isotropic random (IR) on the unit hemisphere, and independent from the uniform random (UR) offset z of the planes along that direction, see Fig. 3.

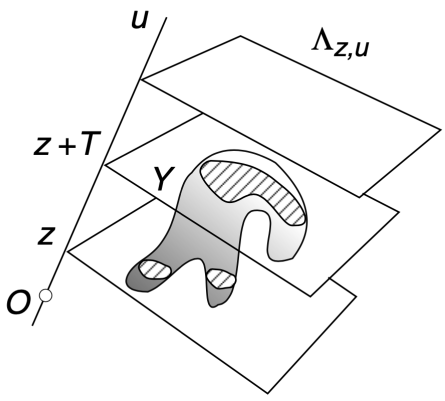

Fig. 3. *Test system of planes hitting a domain D*

For each fixed $u \in \mathbb{S}^2_+$ (non-random), from the Cavalieri estimator and Eq.(12), we have that for $z \sim UR[0,T)$,

$$\widehat{V(D)} = T\, A(D \cap \Lambda_{z,u}) = T \sum A_i, \tag{20}$$

where $A_i = A(D \cap L_2(z+iT,u))$, is an unbiased estimator of $V(D)$.

In a similar way, when $z \sim UR[0,T)$ and $u \sim UR(\mathbb{S}^2_+)$, from Eq.(11), we obtain (see page 205 of Cruz-Orive (2024)) that:

$$\widehat{A(S)} = \frac{4}{\pi}\, T\, \text{Length}(S \cap \Lambda_{z,u}), \tag{21}$$

is an unbiased estimator of A.

Therefore, the stereological estimator of the spherical shape factor is given by:

$$\widehat{F} = \frac{\widehat{A(S)}^3}{36\pi \widehat{V(D)}^2} \tag{22}$$

To obtain an unbiased estimator of E we consider again a test system of planes $\Lambda_{z,u}$. Then, from Eq.(18), we have that

$$\widehat{E} = \frac{16T}{3\pi} \int_{S \cap \Lambda_{z,u} \neq \emptyset} \kappa^2(s)\, ds - \frac{8\pi}{3}. \tag{23}$$

is an unbiased estimator of E.

2D stereological estimators

There are confocal microscopy systems that incorporate the Computer Assisted Stereological Toolbox (CAST), allowing for the direct estimation of geometric parameters from each planar image generated by the microscope, without the need for additional image processing. These estimations are based on point counting over a set of lines sampled randomly (see Figure 4).

Let $\alpha_i(s)$ denote the curve corresponding to the intersection $S \cap L_2(z+iT,u)$, where S is the surface of interest and $L_2(z+iT,u)$ is one of the planes comprising the test system $\Lambda_{z,u}$. We define:

$$A_i = A(D \cap L_2(z+iT,u)),$$

$$B_i = \text{Length}(S \cap L_2(z+iT,u)),$$

and let κ_j be the curvature of α_i at the point $\alpha(t_j)$.

Then, unbiased estimators for A_i and B_i are given by Gual-Vayà (2024):

$$\begin{aligned} \hat{A}_i &= T^2 P, \\ \hat{B}_i &= \frac{\pi}{4} T I, \end{aligned} \tag{24}$$

where P is the number of test points that fall within $D \cap L_2(z+iT,u)$, and I is the number of intersections between the test lines and $S \cap L_2(z+iT,u)$. In Fig. 4, $P = 3$ and $I = 8$.

To approximate the curvature κ_j at each point $\alpha_i(t_j)$, various methods can be employed (see Gual-Arnau et al. (2017)). In this work, we adopt the following approximation:

$$\tilde{\kappa}_i = \frac{4A(T_i)}{a_i b_i c_i}, \tag{25}$$

where T_i denotes the triangle formed by the points

$\alpha(t_{i-1})$, $\alpha(t_i)$, and $\alpha(t_{i+1})$, and a_i, b_i, and c_i are the lengths of the sides of triangle T_i.

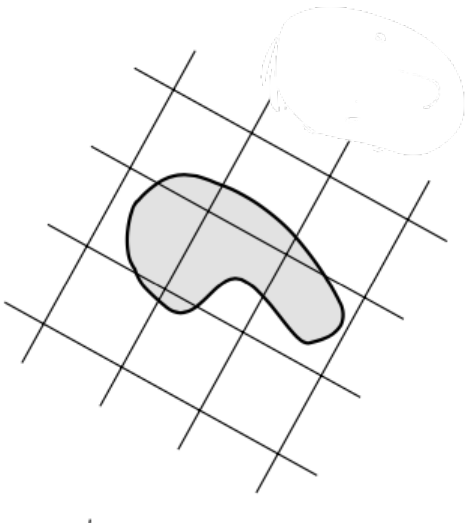

Fig. 4. *A square grid of test lines and a domain in* $\mathbb{R}^2$.

RBC CLASSIFICATION

To classify red blood cells, we will associate two values with each red blood cell, given by the shape factors (F,E). Since the information we will have consists of intersections of the red blood cells with parallel planes given a random direction, instead of the factors (F,E), we will work with their estimates $(\widehat{F},\widehat{E})$.

MODEL GEOMETRIES FOR NORMAL ERYTHROCYTES

There is a consensus in the specialized literature that the most appropriate mathematical model for studying the geometry of normal red blood cells is inspired by the Cassini oval (Canham (1970), Bernard (2016)). This model can be expressed in spherical coordinates as the regular surface resulting from the image of the following parametrizations (Angelov and Mladenov, 2000):

$$x = \frac{\sqrt{(a^2+r^2)^2-c^4}}{2a}\cos\phi,$$

$$y = \frac{\sqrt{(a^2+r^2)^2-c^4}}{2a}\sin\phi,$$

$$z = \pm\frac{\sqrt{c^4-(a^2-r^2)^2}}{2a},$$

where $\phi \in [0,2\pi]$, $r \in [\sqrt{c^2-a^2},\sqrt{c^2+a^2}]$ and a,c are constants which satisfy $a < c < a\sqrt{2}$.

If we define $\varepsilon = \frac{a}{c}$, then, for normal cells, $\varepsilon \in [\frac{1}{\sqrt{2}},1)$. The value of 1 is not considered because the resulting surface is not regular.

Now, based on these parametrizations, we can obtain approximations for the sphericity factors and Bending energy (Angelov and Mladenov, 2000). Table 1 shows the values of these approximations as a function of the parameter ε.

Table 1. *Values of the shape factors for normal cells*

Quantity	Approximation
$F = \frac{A^3}{36\pi V^2}$	$\left(\frac{10-8\varepsilon}{10.38-8.8\varepsilon}\right)^3$
$E = \int_S (\kappa_M^2 + \kappa_m^2)\,dS$	$\frac{151.3-148.23\varepsilon}{10-17.21\varepsilon+7.25\varepsilon^2}$

The values of (F,E) for normal cells depending on the value of ε are given in Table 2.

Table 2. *Values of the shape factors depending on* ε

ε	F	E
1	2.03	76.75
$\frac{5}{6}$	1.31	40.08
$\frac{1}{\sqrt{2}}$	1.14	31.93

In Figure 5, we have the drawings of the surfaces for the values of $\varepsilon = 1/\sqrt{2} \approx 0.71$, $5/6 \approx 0.83$, 0.99 and 0.999.

It is important to note that in the case of the sphere $F = 1$ and $E = 8\pi \approx 25.1327$.

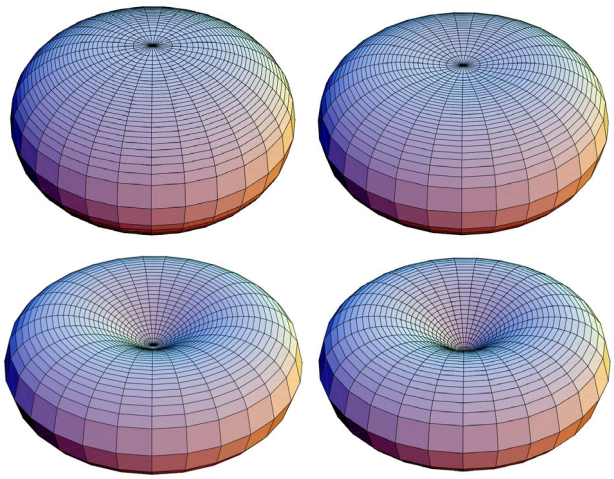

Fig. 5. *Examples of models for normal red blood cells as a function of* ε.

To study the behavior of the shape factor estimates $(\widehat{F},\widehat{E})$, defined in Eqs. (22) and (23), we consider

as an example the model for normal cells with parameters $a = 5$ and $c = 6$. Specifically, we analyze the intersection of the surface generated by this model with planes perpendicular to the y-axis and $T = 1$. In this case, the exact values of the shape factors were $F = 1.31$ and $E = 40.08$ (see Table 2), whereas the stereological estimates obtained using a `MATLAB` code were $\widehat{F} = 1.8656$ and $\widehat{E} = 49.9572$.

Although these estimates depend on the geometric sampling used in the computations, the results suggest that the estimated values of the 3D shape factors introduced in this work are suitable for the classification of red blood cells.

Models for deformed erythrocytes have also been developed. For instance, in the earliest clinically reported cases of sickle cell anemia, red blood cells were observed to adopt crescent and sickle shapes. Since then, additional morphologies have been described, including banana, cigar, and oat-seed shapes, among others Westcott (1987). Other mathematical models for deformed red blood cells, such as echinocytes, can be found in Larkin et al. (2013).

In this work, however, we do not consider models for deformed erythrocytes. Instead, we estimate the values of the shape factors (F, E) for the real dataset introduced in Section 2.

CLASSIFICATION OF A REAL DATA SET OF RBC

The database described in Section 2 consists of a total of 825 red blood cells (RBCs), of which 602 are classified as SDE-type: 93 spherocytes, 41 stomatocytes, 176 discocytes (normal cells), and 292 echinocytes. The remaining 223 cells exhibit other types of deformation, including acanthocytes, keratocytes, knizocytes, multilobate cells, and cell clusters. Figure (6) shows examples of different types of red blood cells. The top row corresponds to SDE cells, while the bottom row includes cells with other deformations (Simionato et al., 2021).

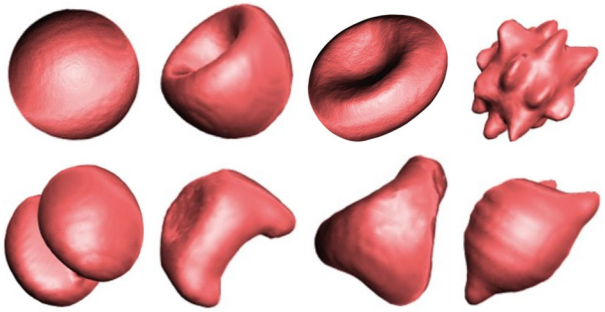

Fig. 6. *Examples of reconstructed cells from the dataset.*

From the planar .tif image files, we developed a custom `Python` code to estimate the values of the shape descriptors F and E, using formulas (22) and (23), respectively. These computations are based on an approximation of the curvature κ at each point along the boundary curves, as described in formula (25). It is important to note that we did not use the 2D stereological estimators (equations 24), since we do not observe the cells directly under the microscope. Instead, we have access to the complete stack of image sections for each individual cell.

The processing pipeline begins by accessing all .tif files corresponding to the image slices of each cell. Each slice is converted to grayscale for simplified intensity analysis, followed by Gaussian filtering to reduce typical confocal noise and binary thresholding at a fixed level to generate a mask isolating fluorescent pixels from the dark background. This enables hierarchical contour detection to delineate both outer boundaries and inner holes (if present) for complete cell shape representation without omissions. Subsequent polygonal approximation then smooths irregular edges while preserving essential morphology, using OpenCV functions, before calculating shape descriptors F and E.

All the resulting F and E values are saved in text format in a single folder, providing a structured dataset that can be readily used for further morphometric analysis or machine learning applications.

To perform the supervised classification tasks described in the following sections, the dataset was split into two subsets: 80% of the data was used for model training, while the remaining 20% was reserved for testing. A fixed random seed was used to ensure reproducibility of the experimental results.

The supervised classification models applied in this study include:

- K-Nearest Neighbors (KNN): using $k = 5$ nearest neighbors.
- Support Vector Machine (SVM): with a Gaussian (RBF) kernel.
- Random Forest (RF): an ensemble of 100 decision trees with fixed random seed (42).
- Logistic Regression (LR): a simple linear model trained with default parameters and fixed seed.
- Gradient Boosting (GB): a sequential ensemble of 100 trees, each correcting the errors of its predecessor.
- Neural Network (MLPClassifier): a multilayer perceptron with two hidden layers of 50 neurons each, trained for a maximum of 1000 iterations.

– Voting Ensemble: a soft-voting ensemble combining RF, GB, and MLP classifiers.

All models yielded comparable accuracy results across the classification tasks. However, Logistic Regression consistently produced the lowest performance, while the Neural Network achieved the highest classification accuracy. Consequently, we provide a more detailed analysis of the Neural Network model in the following sections.

CLASSIFICATION RESULTS

In the first classification task, we aimed to distinguish between healthy red blood cells (discocytes) and all other cell types. The overall classification accuracy achieved was 87%, and the corresponding confusion matrix is shown in Figure 7. Similar results were obtained when grouping SDE cells into one class and all other deformed cells into another, in which case the total classification accuracy was 86%.

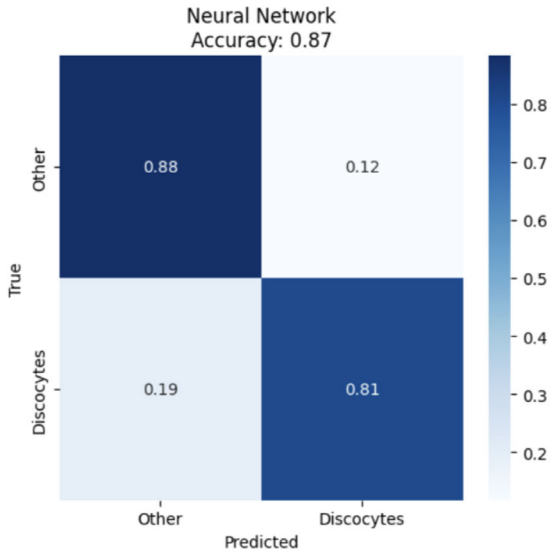

Fig. 7. *Confusion matrix of the first classification process.*

In the second classification task, we focused on distinguishing among the different types within the SDE class. The overall accuracy in this case reached 92%. As shown in the confusion matrix (Figure 8), a significant number of stomatocytes were misclassified as discocytes. This result is not unexpected, as stomatocytes and discocytes lie along a physiological continuum and are interconvertible under normal conditions. Therefore, our model effectively separates discocytes, spherocytes, and echinocytes, but tends to group some stomatocytes with discocytes, a behavior that aligns with the underlying morphological similarity between these two cell types.

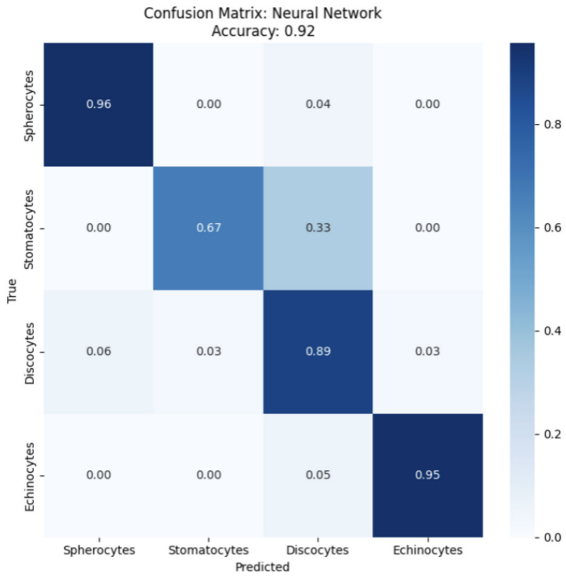

Fig. 8. *Confusion matrix of the second classification process.*

DISCUSSION

In this paper, we introduced two quantitative shape descriptors for red blood cells (RBCs): the well-established spherical shape factor F and a novel descriptor based on bending energy E. When estimated through stereological formulas, these parameters enable the classification of RBCs into morphologically distinct groups, particularly within the classic SDE (stomatocyte–discocyte–echinocyte) spectrum, as well as those exhibiting other deformations.

The classification tasks were performed using supervised learning methods, relying on the stereological estimations $\hat{F}$ and $\hat{E}$. These estimators allow us to approximate global 3D shape properties from randomly sampled planar sections, without requiring full 3D reconstructions. This approach is especially valuable when analyzing confocal microscopy images, where explicit 3D reconstruction can be computationally intensive or infeasible.

While stereological estimators provide an effective bridge between 2D imaging and 3D morphology, they are not without limitations. Both $\hat{F}$ and, in particular, $\hat{E}$ are sensitive to segmentation quality. The bending energy estimator $\hat{E}$ depends heavily on accurately approximating curvature along the planar contours of each section. As a result, fluctuations in the segmentation process may

introduce considerable variability, potentially affecting classification accuracy.

To address this challenge and improve practical applicability, it would be valuable to integrate our estimators into interactive stereology software connected directly to microscopes. This would enable real-time, segmentation-free approximation of shape descriptors, for instance by sampling curvature at a small number of geometrically selected points along the visible cell contours. Such an approach would not only enhance observer efficiency, but also help preserve morphological fidelity and ensure consistency across datasets.

It is also worth noting that, as we had access to a database of fully segmented cell images, we deliberately chose not to apply 2D stereological estimators on individual confocal slices. This decision reflects our methodology's reliance on the full 3D stack of planar sections for robust estimation. Nonetheless, in future applications involving live or semi-automated microscopy, simplified 2D approaches may be reconsidered to improve throughput without significant loss of accuracy.

Overall, our findings confirm the discriminative power of the proposed descriptors and their potential for integration into diagnostic workflows. The spherical shape factor F and the bending energy E capture distinct yet complementary geometric features that reflect membrane mechanics and cellular health. Their application to RBC classification, particularly in distinguishing SDE morphologies, aligns well with known physiological transitions and pathological markers.

ACKNOWLEDGMENDS

The origin of this paper lies in the Master's thesis in Computational Mathematics carried out at Universitat Jaume I (UJI).

REFERENCES

Angelov B and Mladenov I (2000). On the geometry of red blood cell. Geometry, Integrability and Quantization. September 1-10, 1999, Varna, Bulgaria Ivaïlo M. Mladenov and Gregory L. Naber, Editors Coral Press, Sofia:27-46

Bernard Y (2016). Noether's theorem and the Willmore functional. Adv Calc Var 9(3):217-234

Bogdanova A, Kaestner L, Simionato G, Wickrema A, Makhro A (2020). Heterogeneity of Red Blood Cells: Causes and Consequences. Front Physiol 11:392

Canham PB (1970). The Minimum Energy of Bending as a Possible Explanation of the Biconcave Shape of the Human Red Blood Cell J Theor Biol 26:61-81.

Constantino BT (2015). Reporting and grading of abnormal red blood cell morphology. Int J Lab Hematol 37(1):1-7

Cruz-Orive LM (2024). Stereology. Theory and Applications, Interdisciplinary Applied Mathematics, Volume 59, Springer

do Carmo MP (1976). Differential Geometry of Curves and Surfaces. Prentice Hall, Englewood Cliffs, NJ

Foy BH, Stefely JA, Bendapudi PK, Hasserjian RP, Al-Samkari H, Louissaint A, Fitzpatrick MJ, Hutchison B, Mow C, Collins J, Patel HR, Patel CH, Patel N, Ho SN, Kaufman RM, Dzik WH, Higgins JM, Makar RS (2023). Computer vision quantitation of erythrocyte shape abnormalities provides diagnostic, prognostic, and mechanistic insight. Blood Adv 7(16):4621–4630

Gual-Arnau X, Ibáñez Gual MV, Monterde J (2017). Curvature approximation from parabolic sectors. Image Anal Stereol 36(3):233–241

Gual-Vayà Ll (2024). Classification of Red Blood Cells From a Geometric Morphometric Study. Image Anal Stereol 43(1):109–119

Jaferzadeh K, Sim M, Kim N, Moon I (2019). Quantitative analysis of three-dimensional morphology and membrane dynamics of red blood cells during temperature elevation. Sci Rep 9:14062

Khairy K, Foo J, Howard J (2008). Shapes of Red Blood Cells: Comparison of 3D Confocal Images with the Bilayer-Couple Model. Cell Mol Bioeng 1:173–181.

Kim HW, Lee J, Cho M, Lee MC (2022) A study on the classification of red blood cells specimen and data analysis method for the diagnosis of blood disease using a digital holographic microscopy. In: Proc. 13th Int Conf Inf Commun Technol Converg (ICTC), Jeju Island, Republic of Korea, IEEE, pp. 267–271.

Kindratenko VV (2003). On Using Functions to Describe the Shape. J Math Imaging Vis 18:225–245

Kurz A, Müller H, Kather JN, Schneider L, Bucher TC, Brinker TJ (2024). 3-Dimensional Reconstruction From Histopathological Sections: A Systematic Review. Lab Invest 104:102049

Larkin TJ, Pages G, Chapman BE, Rasko JEJ, Kuchel PW (2013). NMR q-space analysis of canonical shapes of human erythrocytes: stomatocytes,

discocytes, spherocytes and echinocytes. Eur Biophys J 42:3–16.

Lin B, Jin D, Socorro-Borges MA (2022). 3D surface reconstruction of the femur and tibia from parallel 2D contours. J Orthop Surg Res 17:145

Liu R, Dey D, Boss D, Marquet P, Javidi B (2011). Recognition and classification of red blood cells using digital holographic microscopy and data clustering with discriminant analysis. J Opt Soc Am A 28:1204-1210.

Pages G, Yau TW, Kuchel PW (2010). Erythrocyte shape reversion from echinocytes to discocytes: Kinetics via fast-measurement NMR diffusion-diffraction. Magn Reson Med 64:645–652

Paz-Soto Y, Herold-Garcia S, Gual-Arnau X, Jaume-i-Capó A, González-Hidalgo M (2025). An efficient heuristic for geometric analysis of cell deformations. Comput Biol Med 186:109709

Ritoré M, Sinestrari C (2010). The classical isoperimetric inequality in Euclidean space. In: Mean Curvature Flow and Isoperimetric Inequalities. Advanced Courses in Mathematics - CRM Barcelona. Birkhäuser Basel

Ruef P, Linderkamp O (1999). Deformability and Geometry of Neonatal Erythrocytes with Irregular Shapes. Pediatr Res 45:114–119

Santaló LA (1976). Integral Geometry and Geometric Probability, Addison-Wesley Publishing Company Inc. London

Simionato G, Hinkelmann K, Chachanidze R, Bianchi P, Fermo E, van Wijk R, Leonetti M, Wagner C, Kaestner L, Quint S (2021). Red blood cell phenotyping from 3D confocal images using artificial neural networks. PLoS Comput Biol 17(5):e1008934

Toda MD (2018). Willmore Energy and Willmore Conjecture, Taylor and Francis. Boca Raton.

Waibel DJE, Kiermeyer N, Atwell S, Sadafi A, Meier M, Marr C (2022). SHAPR predicts 3D cell shapes from 2D microscopic images. iScience, 25(11):105298

Westcott H (1987). Model geometries for sickle erythrocytes. Bull Math Biol 49(4):403-411

Willmore TJ (2002). Riemannian geometry, Oxford University Press, New York